



PACIFIC EARTHQUAKE ENGINEERING RESEARCH CENTER

Evaluation of Numerical Procedures for Simulating Near-Fault Long-Period Ground Motions Using Zeng Method

Yuehua Zeng

John Anderson

University of Nevada, Reno

**A report to the PEER Program of
Applied Earthquake Engineering Research on
Lifeline Systems**

**The financial support of the sponsor organizations including
the Pacific Gas & Electric Company (PG&E),
the California Energy Commission (CEC), and the
California Department of Transportation (Caltrans) is acknowledged.**

ACKNOWLEDGMENTS

The work described in this report was funded by the Pacific Earthquake Engineering Research (PEER) Center under the Pacific Gas & Electric Company Contract No. 09566. This financial support is gratefully acknowledged.

This work made use of Pacific Earthquake Engineering Research Center Shared Facilities supported by the Earthquake Engineering Research Center Program of the National Science Foundation under Award Number EEC-9701568.

The financial support of the PEARL sponsor organizations including the Pacific Gas & Electric Company (PG&E), the California Energy Commission (CEC), and the California Department of Transportation (Caltrans) is acknowledged.

Final Technical Report on Near Fault Ground Motions

Phase II, Task 5: Near-fault ground motions

Yuehua Zeng and John Anderson
Seismological Lab, University of Nevada - Reno

Introduction

Over the past several years, we have developed theories and methods for modeling synthetic strong ground motion using a composite source model (Zeng et al., 1994). The method has been successful in generating realistic strong motion seismograms. The realism is demonstrated by comparing synthetic strong motions with observations from the recent California earthquakes at Landers, Loma Prieta (Su et al., 1994a,b) and Northridge (Zeng and Anderson, 1996; Anderson and Yu, 1996; Su et al., 1998), earthquakes in the eastern US (Ni et al., 1999) and earthquakes in Guerrero, Mexico (Yu, 1994; Johnson, 1999), Turkey (Anderson et al., 1997) and India (Khattari et al, 1994; Zeng et al, 1995). We have also successfully applied the method for earthquake engineering applications to compute the ground motion of scenario earthquakes. During the process of continuing development, we have included scattering waves from small scale heterogeneity structure of the earth, site specific ground motion prediction using weak motion site amplification, and nonlinear soil response using the geotechnical engineering model.

In this report, we investigate the effect of rupture directivity from large damaging earthquakes. First we will find the earthquake source models that best describe the ground motion waveform recorded at the strong motion stations. Then we will use those earthquake source models to simulate near fault ground motion and compared them with the recorded strong motion seismograms. Finally, we will use the near-fault directivity model of Somerville et al. (1997) to test the synthetic prediction of the rupture directivity effect from those earthquake ground motions in term fault normal and fault parallel components.

Method

Composite Source Model

We have developed a composite source model (Zeng et al., 1994) for realistic synthetic strong ground motion seismograms computation. This method uses synthetic Green's functions, which characterize wave propagation in a flat-layered medium, convolved with the composite source time functions. The source is a superposition of circular subevents with constant stress drop. The number of subevents and their radius follows a power law given by

$$\frac{dN}{d(\ln R)} = pR^{-D}$$

where D is the fractal dimension that equals twice the b-value, N is the number of subevents, and p is a constant of proportionality. The random nature of the heterogeneities on a complex fault is simulated by distributing the subevents randomly on the fault plane. Rupture propagates from

the hypocenter at a constant velocity, and each subevent initiates the radiation of a displacement pulse of a crack model. The heterogeneous nature of the composite earthquake faulting is apparently characterized by the maximum subevents size and the subevents stress drop, which can be constrained by other independent geophysical data.

The synthetic Green's function has been modified to consider the effect of the random lateral heterogeneity of the earth by adding scattered waves into the Green's function (Zeng, 1995). The solution is then convolved with a plane wave propagation function through a near surface 1-D velocity layering as complex as that suggested by sonic well logs. Thus the complex high-frequency waveform of our simulation is generated from a combination of a heterogeneous source (Figure 1), wave reverberation in a stratified crustal structure (Figure 2) and scattering from lateral inhomogeneity of the earth (Figure 3).

Earthquake source Imaging Using Genetic Algorithm

Zeng and Anderson (1996) used a Genetic Algorithm to find a specific composite source model that best fit the observed waveform data for the Northridge earthquake. The Genetic Algorithm works by mimicking the process of natural selection principle of survival of the fittest. By analogy with the natural behavior, it starts with an initial "population" of "individuals" (e.g., models of the subevent locations), each representing a possible solution. A fitness score is assigned to each individual. Individuals with higher fitness are given better opportunities to "crossbreed" with others in the population to produce "offspring" that form a new population the same size as the original. The algorithm iterates by taking those offspring as a new generation and repeats the process until a satisfactory solution is obtained.

The fitness function in our waveform inversion is defined as

$$F(m^i) = \sum_{\substack{\text{stations and} \\ \text{components}}} \frac{\min(u_{\max}^o, u_{\max}^s)}{\max(u_{\max}^o, u_{\max}^s)} \left(\frac{\sum_l u_l^o u_l^s}{\sqrt{\sum_l u_l^o u_l^o} \sqrt{\sum_l u_l^s u_l^s}} \right)$$

where m^i is the i th individual; u_l^o is the observed seismogram; u_l^s is the corresponding synthetic seismogram; and u_{\max}^o and u_{\max}^s are the corresponding peak values of the observed and synthetic seismograms, respectively. The representation in the parentheses gives the cross-correlation coefficient of the synthetic with the data. The weights given to the correlation coefficients penalize seismograms with similar waveforms but different amplitudes. Each individual is assigned a fitness value based on the above equation.

Next, we pick two individuals as "parents" for a reproduction event using the so-called roulette wheel selection scheme. The two parents are used to generate two offspring by recombining their "chromosomes" using the mechanisms of cross-over and mutation. The chromosomes in our case are the subevent locations on the rupture plane. The subevents of both models are divided randomly into 10 groups exactly, and their positions are copied into their offspring according to a randomly generated "cross-over mask." Mutation is applied to each offspring individually after cross-over. It is done by randomly altering the location of each subevent with a probability of 0.01.

Modified Source Radiation

Motivated by the fact that we do not observe any distinct radiation pattern and wave polarization at high frequency, we introduced an effective high frequency source radiation term.

This source radiation consists of energy contributions from an angular cross section centered at the direction from the source to receiver in order to simulate high frequency wave reflection and scattering at the fault zone. The total source radiation then equals

$$\alpha \cdot \text{effective-source-radiation} + (1 - \alpha) \cdot \text{double-couple-source-radiation},$$

where α is a continuo function of frequency. It equals 1 above a high frequency threshold and tapers to 0 at low frequency since this reflection and scattering at the source zone has less an effect at lower frequencies (Figure 4). The results were validated with the Northridge strong motion observations. We have compared the results with the observed and regression prediction (Abrahamson and Silva, 1997) of the PGA and SA at 3 second. The synthetic simulations clearly predict the trends of the observed ground motion parameters better than the regression. The scatter in the data is presumably caused by local site and basin response effects.

Data and Analysis

We selected several important earthquakes for the validation study of the composite source model. These events are selected through PEER and PG&E project coordination meeting. A list of those events is given in Table 1.

Table 1. Earthquakes used for the model validation

Event year	Event name	Epicenter Latitude	Epicenter Longitude	Hypocenter Depth
1979	Imperial Valley earthquake, CA	32.6435	115.3088	8.0
1989	Loma Prieta earthquake, CA	37.0407	121.8829	17.6
1992	Landers earthquake, CA	34.2000	116.4300	7.0
1994	Northridge earthquake, CA	34.215	118.538	17.5
1995	Kobe earthquake, Japan	34.5948	135.0121	16.9

Near field strong motion seismograms from those events within about 40 km of the fault planes were selected. Table 2a, 2b, 2c, 2d and 2e list the station names, locations for the strong motion data analysis of the 5 earthquakes listed in Table 1, respectively. The total number of strong motion stations selected for Imperial Valley, Loma Prieta, Landers, Northridge, and Kobe earthquakes are 28, 34, 13, 33 and 15, respectively.

Table 2a

Station names and locations for the Imperial Valley earthquake

Name	Latitude	Longitude	Description
AEPI	32.6510	-115.3320	Aeropuerto Mexicali
AGRI	32.6210	-115.3010	Agrarias
BCRI	32.6930	-115.3380	Bonds Corner
BRAI	32.9910	-115.5120	Brawley Airport
CXOI	32.6690	-115.4920	Calexico Fire Station
CALI	33.1300	-115.5200	Calipatria Fire Station
CPEI	32.4200	-115.3010	Cerro Prieto
CHII	32.4840	-115.2400	Chihuahua
ECCI	32.7930	-115.5620	El Centro - Imp County Center FF

EMOI	32.7730	-115.4470	El Centro - Meloland Overpass FF
E01I	32.9600	-115.3190	El Centro #1
E03I	32.8940	-115.3800	El Centro #3
E04I	32.8640	-115.4320	El Centro #4
E05I	32.8550	-115.4660	El Centro #5
E06I	32.8390	-115.4870	El Centro #6
E07I	32.8290	-115.5040	El Centro #7
E08I	32.8110	-115.5320	El Centro #8
E10I	32.7800	-115.5670	El Centro #10
E11I	32.7520	-115.5940	El Centro #11
E12I	32.7180	-115.6370	El Centro #12
E13I	32.7090	-115.6830	El Centro #13
EDAI	32.7960	-115.5350	El Centro Diff Array #1
HVPI	32.8120	-115.3770	Holtville Post Office
PTSI	32.9290	-115.6990	Parachute Test Site
PLSI	32.7900	-115.8600	Plaster City
SHPI	32.6180	-115.4280	SAHOP Casa Flores
SUPI	32.9550	-115.8230	Superstition Mountain
WSMI	33.0370	-115.6230	Westmoreland

Table 2b

Station names and locations for the Loma Prieta earthquake

<u>Name</u>	<u>Latitude</u>	<u>Longitude</u>	<u>Description</u>
AGWI	37.3970	-121.9520	Agnews State Hospital
ANDI	37.1650	-121.6310	Anderson Dam (downstream)
ADLI	37.1650	-121.6320	Anderson Dam, L Abut
A07I	37.4900	-122.3100	APEEL 7 - Pulgas
A09I	37.4700	-122.3200	APEEL 9 - Crystal Springs Res
A10I	37.4650	-122.3430	APEEL 10 - Skyline
BESI	37.5120	-122.3080	Belmont - Envirotech
BRNI	37.0470	-121.9850	BRAN
CAPI	36.9740	-121.9520	Capitola
CLSI	37.0460	-121.8030	Corralitos
CLDI	37.1240	-121.5510	Coyote Lake Dam (Downstr)
CYCI	37.1180	-121.5500	Coyote Lake Dam (SW Abut)
GILI	36.9730	-121.5680	Gilroy Gavilan College
GOFI	37.0090	-121.5690	Gilroy, Historic Bldg
G01I	36.9730	-121.5720	Gilroy #1
G02I	36.9820	-121.5560	Gilroy #2
G03I	36.9870	-121.5360	Gilroy #3
G04I	37.0050	-121.5220	Gilroy #4
G06I	37.0260	-121.4840	Gilroy #6
GMRI	37.0330	-121.4340	Gilroy #7
HCHI	36.8510	-121.4020	Hollister City Hall
HDAI	36.8880	-121.4130	Hollister Differential Array
HSPI	36.8480	-121.3970	Hollister-South & Pine
LGPI	37.1720	-122.0100	LGPC
PAEI	37.4530	-122.1120	Palo Alto - 1900 Embarcadero
SLCI	37.4190	-122.2050	Palo Alto - SLAC
SJWI	36.6710	-121.6420	Salinas
STGI	37.2550	-122.0310	Saratoga-Aloha
WVCI	37.2620	-122.0090	Saratoga WVC
SVLI	37.4020	-122.0240	Sunnyvale - Colton Ave
UC2I	37.0000	-122.0620	UCSC
LOBI	37.0370	-121.8830	Santa Cruz UCSC/Lick

WAHI 36.9720 -121.9950 UCSC WAHO
WDSI 37.4290 -122.2580 Woodside

Table 2c

Station names and locations for the Landers earthquake

Name	Latitude	Longitude	Description
BRSL	34.8870	-117.0470	BARSTOW
DSPL	33.9620	-116.5090	DESERT HOT SPRINGS
INDL	33.7170	-116.1560	INDIO - COACHELLA CANAL
JOSL	34.1310	-116.3140	JOSHUA TREE
LCNL	34.5680	-116.6120	LUCERNE
MCFL	34.9050	-116.4190	MISSION CREEK FAULT
MVHL	34.0480	-116.5770	MORONGO VALLEY
NPSL	33.9240	-116.5430	NORTH PALM SPRINGS
PSAL	33.8290	-116.5010	PALM SPRINGS AIRPORT
SILL	33.8510	-116.8520	SILENT VALLEY - POPPET FLAT
29PL	34.0210	-116.0090	TWENTY NINE PALMS
YERL	34.9030	-116.8230	YERMO FIRE STATION
CLWL	34.8520	-116.8580	COOLWATER

Table 2d

Station names and locations for the Northridge earthquake

Name	Latitude	Longitude	Description
ARLN	34.236	-118.439	ARLETA - SAN FERNANDO
TUJN	34.286	-118.225	BIG TUJUNGA STATION USC #61
BVAN	34.063	-118.463	BRENTWOOD VA HOSP BLDG 259
HOWN	34.204	-118.302	BURBANK 1250 HOWARD RD
CNPN	34.212	-118.605	CANOGA PARK 7769 TOPANGA CANYON BLVD
LOSN	34.419	-118.426	CANYON COUNTRY 16628 W LOST CANYON RD
ORRN	34.564	-118.642	CASTAIC - OLD RIDGE ROUTE
GLPN	34.2	-118.231	GLENDALE 3320 LAS PALMAS AVE
JENN	34.312	-118.496	JENSEN FILTRATION PLANT ADMIN. BLDG
LDMN	34.295	-118.479	LA DAM FOUNDATION
WONN	34.114	-118.38	LOS ANGELES 8510 WONDERLAND AVE
NYAN	34.238	-118.253	LA CRESCENTA 4747 NEW YORK AVE
L09N	34.608	-118.558	LAKE HUGHES #9
H12N	34.57	-118.56	LAKE HUGHES ARRAY #12
MRPN	34.288	-118.881	MOORPARK
CWCN	34.194	-118.411	NORTH HOLLYWOOD 6850 COLDWATER CANYON
NWHN	34.387	-118.530	NEWHALL - LA COUNTY FIRE STATION
WPIN	34.391	-118.621	NEWHALL W PICO CANYON BLVD
STCN	34.209	-118.517	NORTHRIDGE 17645 SATICOY ST
PACN	34.334	-118.396	PACOIMA DAM - DOWN STREAM
PKCN	34.288	-118.375	PACOIMA - KAGEL CANYON
RRSN	34.281	-118.478	RINALDI RECEIVING STATION
SSUN	34.231	-118.713	SANTA SUSANA ETEC LIQUID METAL ENG CTR
SPVN	34.249	-118.478	SEPULVEDA VA HOSP
KATN	34.264	-118.666	SIMI VALLEY 6334 KATHERINE RD
SCRN	34.106	-118.454	STONE CANYON RES DAM
RO3N	34.221	-118.421	SUN VALLEY 13248 ROSCOE BLVD
GLEN	34.269	-118.303	SUNLAND 10965 MT GLEASON AVE

SCSN	34.311	-118.49	SYLMAR CONVERTER STATION
SCEN	34.312	-118.481	SYLMAR CONVERTER STATION EAST
SYLN	34.326	-118.444	SYLMAR OLIVE VIEW MEDICAL CENTER
TPFN	34.084	-118.599	TOPANGA FIRE STATION
VASN	34.492	-118.327	VASQUEZ ROCKS PARK
PARN	34.44	-118.58	Pardee - SCE

Table 2e

Station names and locations for the Kobe earthquake

Name	Latitude	Longitude	Description
ABNK	34.636	135.519	ABENO (ABN)
AMAK	34.718	135.408	AMAGASAKI (AMA)
FKSK	34.687	135.474	FUKUSHIMA (FKS)
KAKK	34.725	134.843	KAKOGAWA (KAK)
KBUK	34.725	135.240	KOBE UNIVERSITY (KBU)
KJMK	34.688	135.180	KJMA (KJM)
MRGK	34.680	135.572	MORIGAWACHI (MRG)
NISK	34.664	134.964	NISHI-AKASHI (NIS)
OSAK	34.678	135.520	OSAJ (OSA)
SKIK	34.564	135.469	SAKAI (SKI)
SHIK	34.737	135.516	SHIN-OSAKA (SHI)
TDOK	34.480	135.408	TADOKA (TDO)
TAZK	34.809	135.344	TAKARAZUKA (TAZ)
TAKK	34.649	135.139	TAKATORI (TAK)
YAEK	34.680	135.612	YAE
CHYK	34.439	135.659	CHICAYA (CHY)
PRIK	34.670	135.201	PORT ISLAND (0 M) (PRI)
KP2K	34.670	135.201	PORT ISLAND (16 M) (KP2)
KP3K	34.670	135.201	PORT ISLAND (32 M) (KP3)
KP4K	34.670	135.201	PORT ISLAND (83 M) (KP4)
TOTK	34.240	134.240	TOT

We filtered all the seismograms using a 4th order non-causal Butterworth filter with a pass band specified between 8 to 0.7 second period range. The S-wave arrival times of the strong motion records were picked and matched with the theoretical calculations based on a flat-layered crustal velocity model of the region. The crustal velocity model for the Imperial Valley, Landers and Northridge earthquakes are modified from Wald et al. (1996). The crustal velocity model for the Loma Prieta earthquake is modified from Somerville and Yoshimura (1990). The velocity model for the Kobe, Japan, earthquake is modified from Wald (1996). The modification is to add a 30 meters low velocity layer and a 100 meters transition layer on top of those regional velocity models to accommodate the site condition at each station. The site classifications for all strong motion stations are provided by Walt (1999, personal communication). The average shear wave velocity of the top 30 meter surface layer is assigned according to the USGS published site classification using shear wave velocities. These results are then used to calculated source inversion to determine the source rupture process of those earthquake events.

Earthquake Models

Using the Genetic Algorithm inversion, we inverted the strong motion data to obtain the earthquake source rupture processes of the earthquake events listed in Table 1.

We first studied the Imperial Valley earthquake source rupture process using the composite source model. This earthquake occurred on October 15, 1979 and has generated a large amount of strong motion records. A total of 28 stations were selected for the source inversion. Figure 5a shows a map view of the station and fault geometry distribution. We used the same fault geometry and seismic moment for the event as that of Hartzell and Heaton (1983). Figure 5b shows the slip distribution of this earthquake plotted in both slip vector and amplitude intensity scale. We found one large slip zone in the center on the fault. This result is consistent with the solution obtained by Hartzell and Heaton for the Imperial Valley earthquake source rupture process using teleseismic and strong motion inversion. From the slip vector distribution, we can see that this earthquake is almost a pure strike slip event. There is little or even no slip near the hypocenter area. Hartzell and Heaton have suggested that rupture has been accelerated from the hypocenter northward. The large slip in the middle of the fault could be a triggered event by a smaller rupture event near the hypocenter.

The Loma Prieta earthquake struck the San Francisco Bay area on October 17, 1989 and ruptured a 40 km segment of the San Andreas fault in the southern Santa Cruz area. Figure 6a is a map view of the fault geometry and the distribution of the strong motion stations used for the waveform inversion. There are total 34 station were selected for the waveform inversion to find a specific composite source model of the Loma Prieta earthquake. The seismic moment of this earthquake is estimated at 2.9×10^{26} dyne-cm. Figure 6b plots the slip distribution in vector and amplitude intensity scale. The result shows a large slip source located on the southeast side of the fault and another large slip source on the northwest side of the fault. Slip orientation changes from pure strike slip on the southeast side of the fault to oblique slip on the northwest side of the rupture plane. This solution agrees very well with Wald et al. (1991) and other studies of the Loma Prieta earthquake using different techniques. Strong nonlinear soil responses have been observed at site of strong motion station (Chin and Aki, 1992). The effect of the nonlinearity is not considered in the present investigation.

The 28 June 1992 Landers earthquake (Mw 7.2) ruptured through the fault of 70 km long with a long duration of around 24 second. A map view of the fault geometry and strong motion stations used for this source inversion is shown in Figure 7a. A total of 13 stations were used for the study. The seismic moment of this event is estimated to be 7.7×10^{26} dyn-cm. Figure 7b plots the distribution of slip vector and amplitude over the fault plane. Our inversion solution differs from Wald et al. (1994) and shows large slip zones near the centers of the three fault segments. Location of minimum fault slips coincide well with the ends or stepping sections of the fault, suggesting that fault stepovers act like barriers to the source dynamic rupture.

The 17 January 1994 Northridge earthquake (Mw 6.7) occurred on a buried thrust fault in the northwest Los Angeles metropolitan area. Zeng and Anderson (1996) studied this earthquake rupture process using the Genetic Algorithm and the composite source model. This study differs from the previous investigation by using a variable rake for the fault slip and a total of 33 strong motion records instead of 10 seismograms (Figure 8a). We used the same fault geometry as that of Wald et al. (1996). The seismic moment of this earthquake is estimated to be 1.4×10^{26} dyne-cm. Figure 4a shows a map view of the station and fault geometry distribution. Figure 8b plots the earthquake slip distribution of the composite source model and the slip vector distribution over the fault plane. The result indicates a complex earthquake rupture process with three large slip zones: one above the hypocenter, and two others located to the west of the hypocenter. This result is essentially the same as our previous study.

Near fault strong motion records of the January 17, 1995 Kobe, Japan earthquake were

also used to study the rupture process of the source. Figure 9a shows a map view of the station distribution and fault geometry. A total of 15 strong motion seismograms within about 30 km of the fault were selected. We applied Genetic Algorithm to find the specific composite source model that best fit the observed strong motion waveforms. We used the same fault geometry of Wald (1996). The moment of the earthquake is estimated about 2.4×10^{24} dyne-cm. Figure 9b shows the resulting slip and rake distribution of the composite source model determined from the waveform inversion. The plot suggests that much of the earthquake moment was released at shallow depths of the first fault segment. However, the smaller slip sources from the second fault segment actually causes more damage to the surface structures.

Rupture directivity

With the earthquake source model derived above, we then test the effect of rupture directivity of the composite source model comparing with the observation. Such an effect will be examined using different fitness functions. However, the effect of predicted directivity is not measured by the absolute value of those fitness parameters. Instead, we are looking for the trend of those values related to the directivity model parameter.

Somerville et al. (1997) have parameterized the rupture directivity as a function of $X \cdot \cos(\theta)$ for strike slip fault and $Y \cdot \cos(\phi)$ for dip slip fault, where X and Y represent the fraction of the rupture between the hypocenter and the station, θ represents the angle between the fault strike and the line connecting the epicenter to the station, and ϕ represents the angle between the dip direction of the fault to the line connecting the hypocenter to the station. Figure 10 is reproduced from Somerville et al. (1997) to illustrate the meaning of those variables for the directivity model. Thus the smaller the angle between rupture propagation and wave propagation, the larger the rupture directivity effect. Also the large the fraction of the fault lies between the hypocenter and station, the large the rupture directivity.

For the fitness parameter, we will use the weighted cross-correlation. This parameter provides good measure of the match in phase between synthetic prediction and the observation. However, a large difference in amplitude between synthetics and observation may result in the same cross-correlation. This is remedied by introducing a weighting parameter we have discussed earlier in the method section. We will also use the ratio of the synthetic and the observed response spectrum at different periods to test the rupture directivity.

Figure 11 plots the weighted cross-correlations versus the directivity parameter defined by Somerville et al. (1997). Symbols in different colors represent values computed for different earthquakes. The solid line represents a moving average for all parameters. The dotted lines are \pm two mean-standard-error from the average cross-correlation. The top panel of the plot is for fault parallel and the lower panel of the plot is for fault normal. Figure 12, 13 and 14 are the same figure but for spectral ratio of the observation and the synthetics at 1, 3, and 5 seconds. There are slight over prediction at the zero fault directivity, especially for the normal component. Overall, by carefully examine the trend of those ratio versus directivity parameter for all stations, we did not find any significant bias or trends in the results. This suggests that the composite source model predicts the observed directivity very well.

Conclusion

1. We have used Genetic Algorithm to find a specific composite source model for each large earthquake used for the near field ground motion analysis. The models give best fit to the

ground motion waveform in terms of the weighted cross-correlation between synthetics and observations.

2. Our composite source slip models agree with results from other studies using different earthquake source modeling methods for Loma Prieta, Imperial Valley, Northridge and Kobe events. For Landers event, Our model shows large slip occurred near the centers of the fault segments. Locations of minimum slips on the fault coincide with the segment boundaries, suggesting fault stepovers act as barriers to earthquake rupture.

3. In terms of near fault rupture directivity, our error analysis shows the composite source model simulations are consistent with the observed directivity effects. We did not find any significant bias trends in terms of the weighted cross-correlation and response spectrum ratios between synthetics and observations.

Reference

- Abrahamson, N. A. and W. J. Silva (1997). Equations for estimating horizontal response spectra and peak acceleration from western North American earthquakes: a summary of recent work, *Seism. Res. Lett.*, 68, 94-127.
- Anderson, J. G. and G. Yu (1996). Predictability of strong motions from the Northridge, California, earthquake, *Bull. Seism. Soc. Am.* No. 86, 1B, S100-S114.
- Anderson, J. G., Y. Zeng, H. Sucuoglu (1997). Analysis accelerations from the Dinar, Turkey earthquake, presented at the Eighth International Conference on Soil Dynamics and Earthquake Engineering at Istanbul, Turkey.
- Chin, B. H. and K. Aki (1991). Simultaneous study of the source, path and site effects on strong ground motion during the 1989 Loma Prieta earthquake: A preliminary result on pervasive nonlinear site effects, *Bull. Seism. Soc. Am.* No. 81, 1859-1884.
- Hartzell, S. H. and T. H. Heaton (1983). Inversion of strong ground motion and teleseismic waveform data for the fault rupture history of the 1979 Imperial Valley, California, earthquake, *Bull. Seism. Soc. Am.* No. 73, 6, 1553-1583.
- Johnson, M. (1999). Composite source model parameters for large earthquakes ($M > 5.0$) in the Mexican subduction zone, M. S. thesis, University of Nevada, Reno.
- Khattri, K. N., Y. Guang, J. G. Anderson, J. N. Brune and Y. Zeng (1994). Seismic hazard estimation using modelling of earthquake strong ground motions: A brief analysis of 1991 Uttarkashi earthquake, Himalaya and prognostication for a great earthquake in the region, *Current Science*, 67, 343-353
- Ni, S.-D., J. G. Anderson, Y. Zeng (1999). Comparison of strong ground motions from the 1988 Seguenay earthquake with the synthetic simulations using the composite source model, in preparation.
- Somerville, P. G. and J. Yoshimura (1990). The influence of critical Moho reflections on strong ground motions recorded in San Francisco and Oakland during the 1989 Loma Prieta earthquake, *Geophys. Res. Lett.*, 17, 1203-1206.
- Somerville, P. G., N. F. Smith, R. W. Graves, and N. A. Abrahamson (1997). Modification of empirical strong ground motion attenuation relations to include the amplitude and duration effects of rupture Directivity, *Seism. Res. Lett.*, 68, 199-222.
- Su, Feng, Y. Zeng and J. G. Anderson (1994a). Simulation of the Loma Prieta earthquake strong ground motion using a composite source model, *EOS, Trans. A.G.U.*, 75, 44, p448.
- Su, F., Y. Zeng and J. G. Anderson (1994b). Simulation of Landers earthquake strong ground motion using a composite source model, *Seism. Res. Lett.*, 65, p52.

- Su, F., J. G. Anderson and Y. Zeng (1998). Study of weak and strong motion including nonlinearity in the Northridge, California, earthquake sequence, submitted to *Bull. Seis. Soc. Am.* **88**, 1411-1425.
- Wald, D. J., T. H. Heaton, and D. V. Helmberger, (1991), Rupture model of the 1989 Loma Prieta earthquake from the inversion of strong motion and broadband teleseismic data, *Bull. Seism. Soc. Am.*, 81, 1540-1572, 1991.
- Wald, D. J., and T. H. Heaton (1994), Spatial and temporal distribution of slip for the 1992 Landers, California, earthquake, *Bull. Seism. Soc. Am.*, 84, 668-691, 1994.
- Wald, D. J., T. H. Heaton, and K. W. Hudnut (1996). The slip history of the 1994 Northridge, California, earthquake determined from strong-motion, teleseismic, GPS, and Leveling data, *BSSA*, 86, S49-S70.
- Wald, D. J. (1996). Slip history of the 1995 Kobe, Japan, earthquake determined from strong ground motions, teleseismic, geodetic data, *J. Physics of the Earth*, 44, 489-504.
- Yu, G., 1994. Some aspects of earthquake seismology: slip partitioning along major convergent plate boundaries; composite source model for estimation of strong motion; and nonlinear soil response modeling, PH.D Thesis, *University of Nevada*, Reno, Nevada.
- Zeng, Y., J. G. Anderson and G. Yu (1994). A composite source model for computing realistic synthetic strong ground motions, *J. Res. Lett.*, **21**, 725-728.
- Zeng, Y., J. G. Anderson and Feng Su (1995). Subevent rake and scattering effects in realistic strong ground motion simulation, *Geophy. Res. Lett.*, **22**, 17-20.
- Zeng, Y. (1995). A realistic synthetic Green's function calculation using a combined deterministic and stochastic modeling approach, *EOS, Trans. A.G.U.*, **76**, F357.
- Zeng, Y. and J. G. Anderson (1996). A composite source modeling of the 1994 North-ridge earthquake using Genetic Algorithm, *Bull. Seism. Soc. Am.* 86, No. 1B, 71-83.

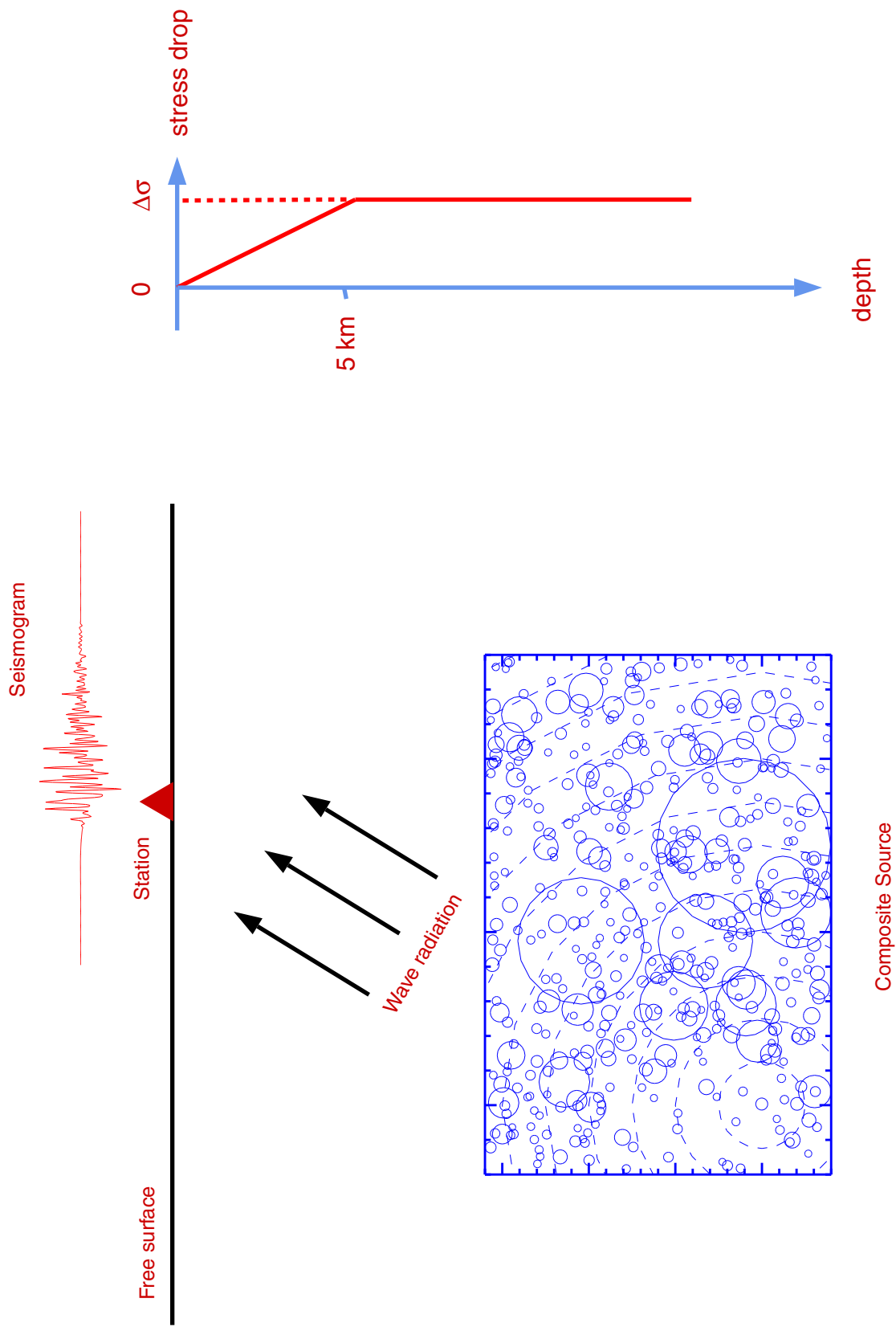


Figure 1. Schematic plot of the complexity in wave field caused by composite source of earthquake.

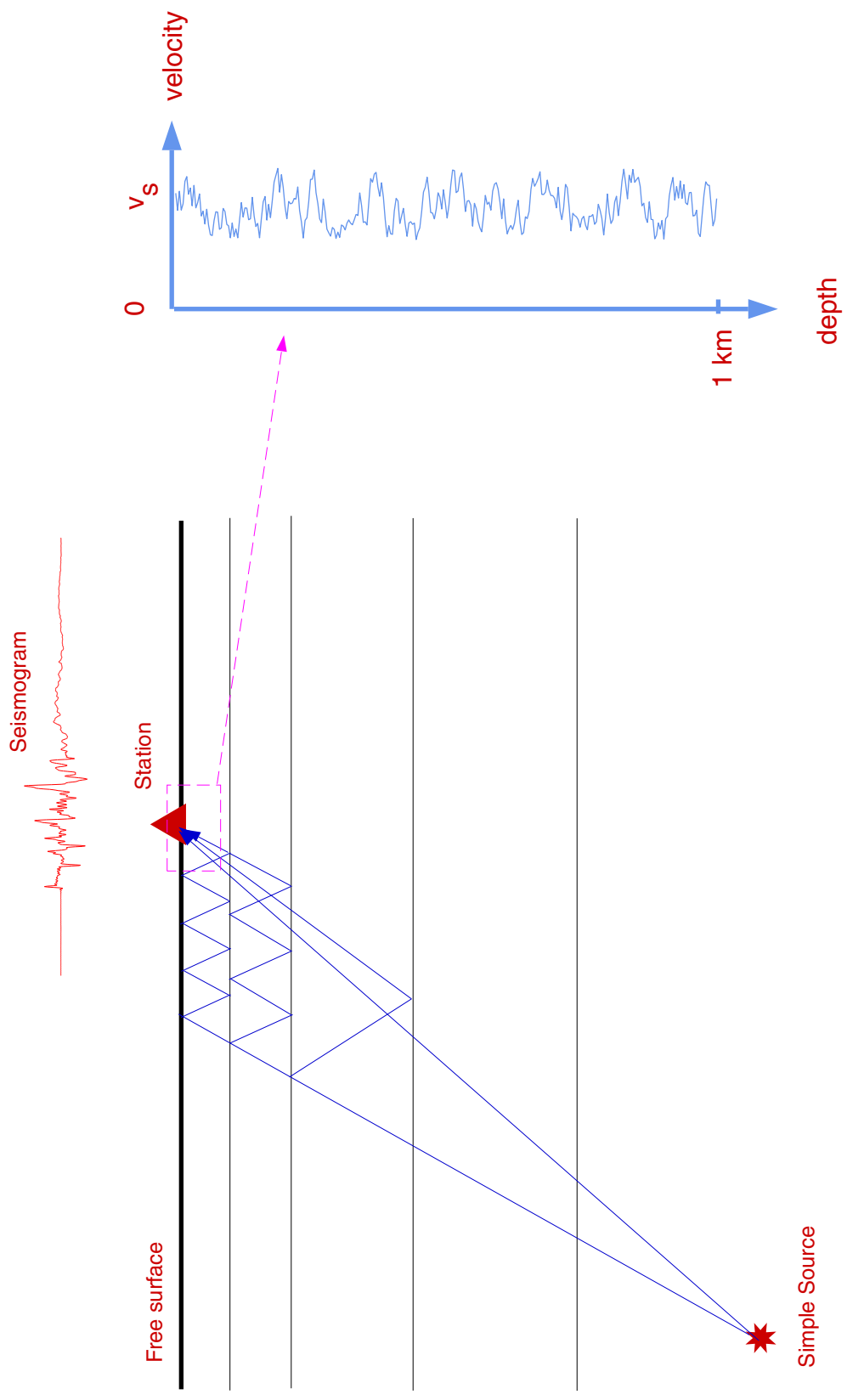


Figure 2. Schematic plot of the complexity in wave field caused by reverberation of waves in a vertically inhomogeneous structure of the earth.

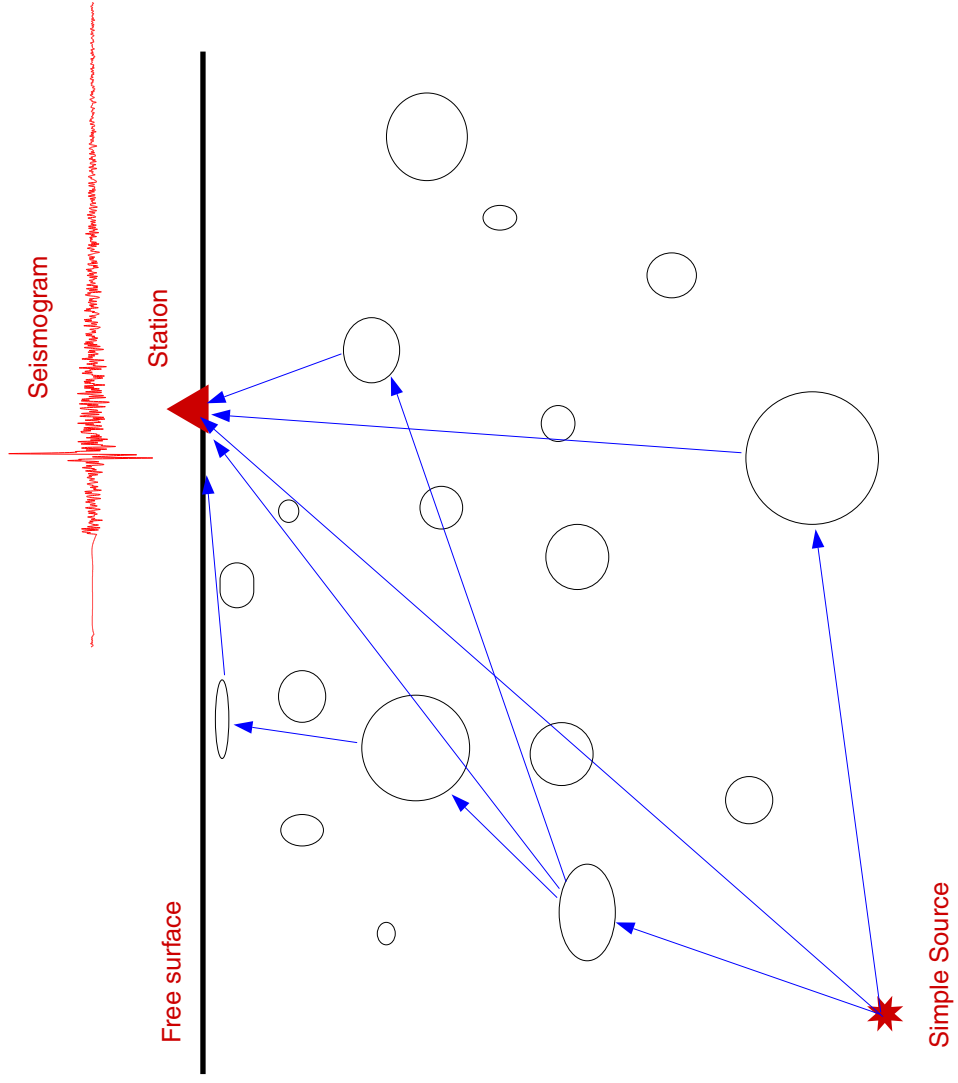
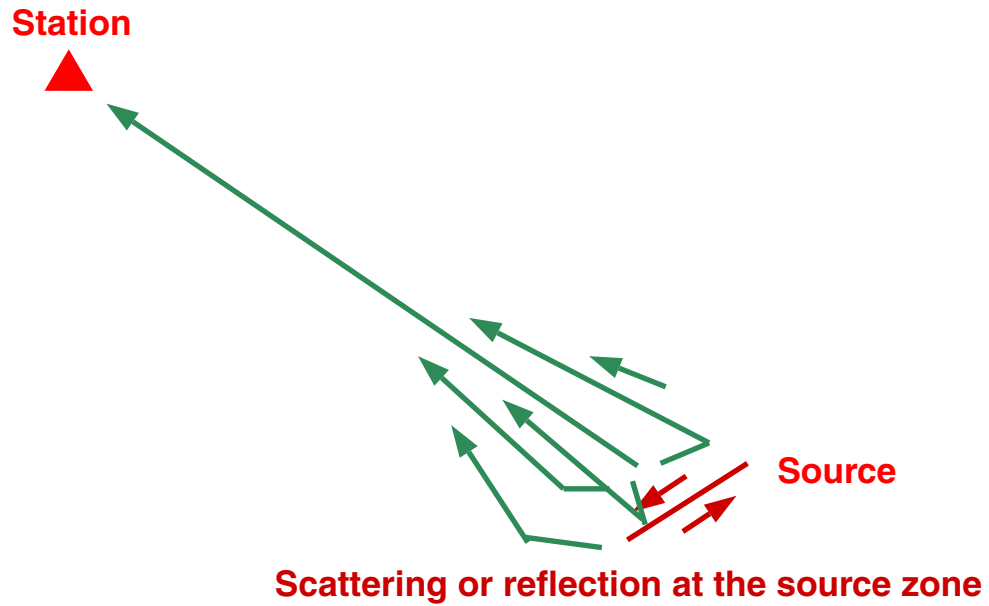


Figure 3. Schematic plot of the complexity in wave field caused by scattering waves from a laterally inhomogeneous structure of the earth.

Source Radiation:



Total source radiation =

$$\alpha \times \text{Effective-source-radiation} + (1 + \alpha) \times \text{double-couple-source}$$

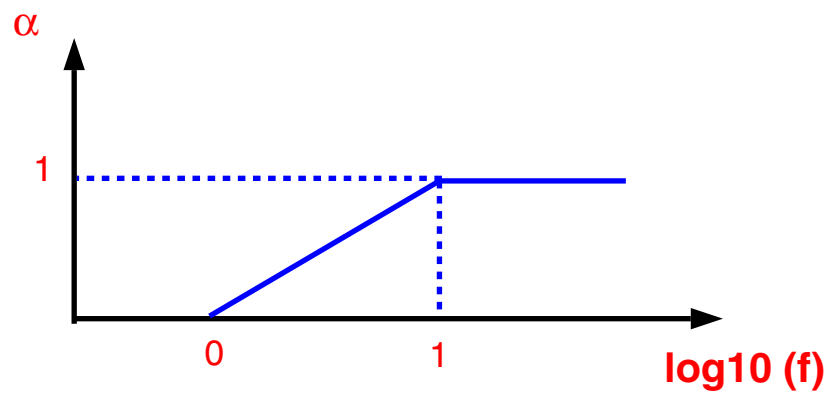
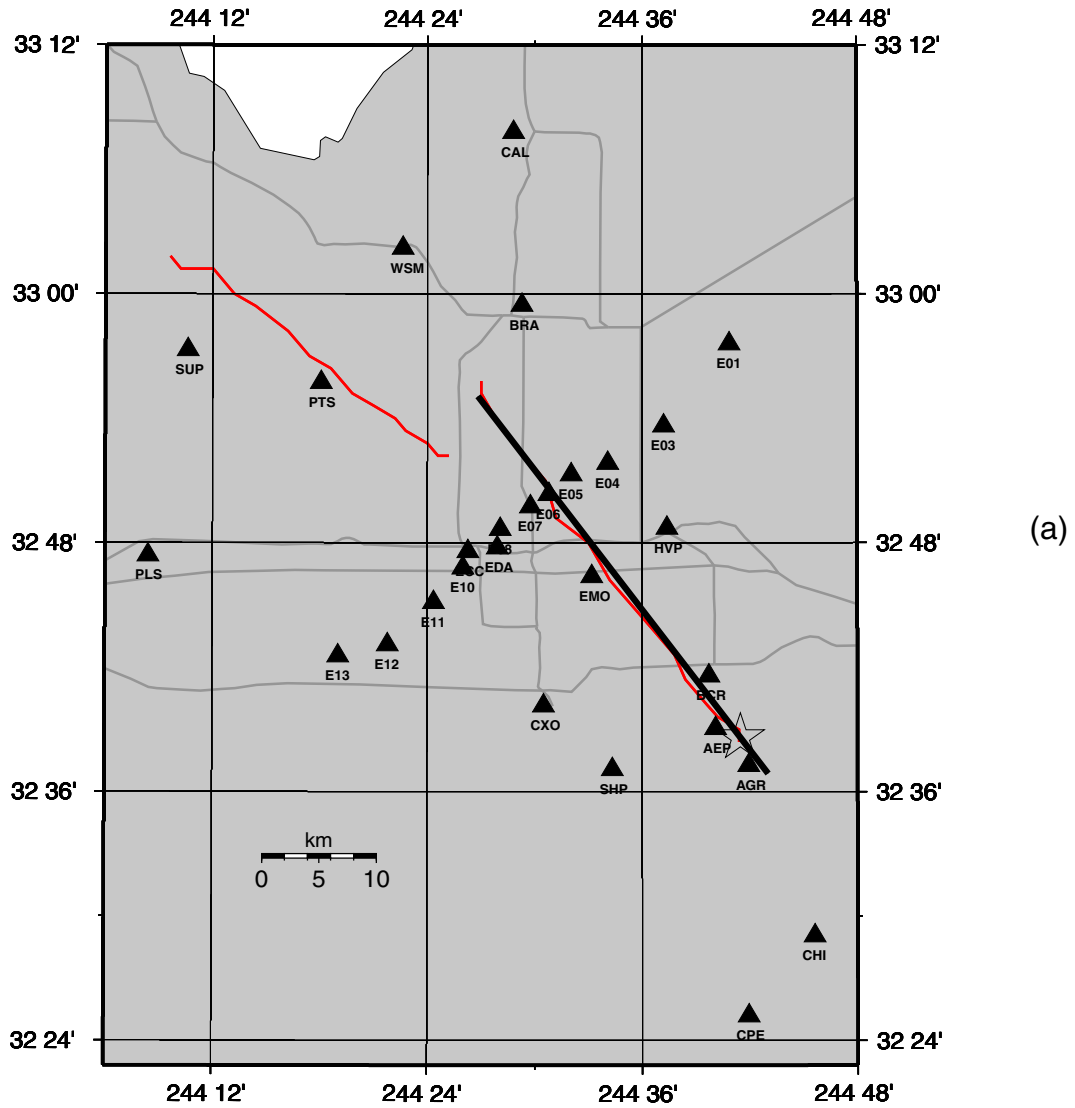
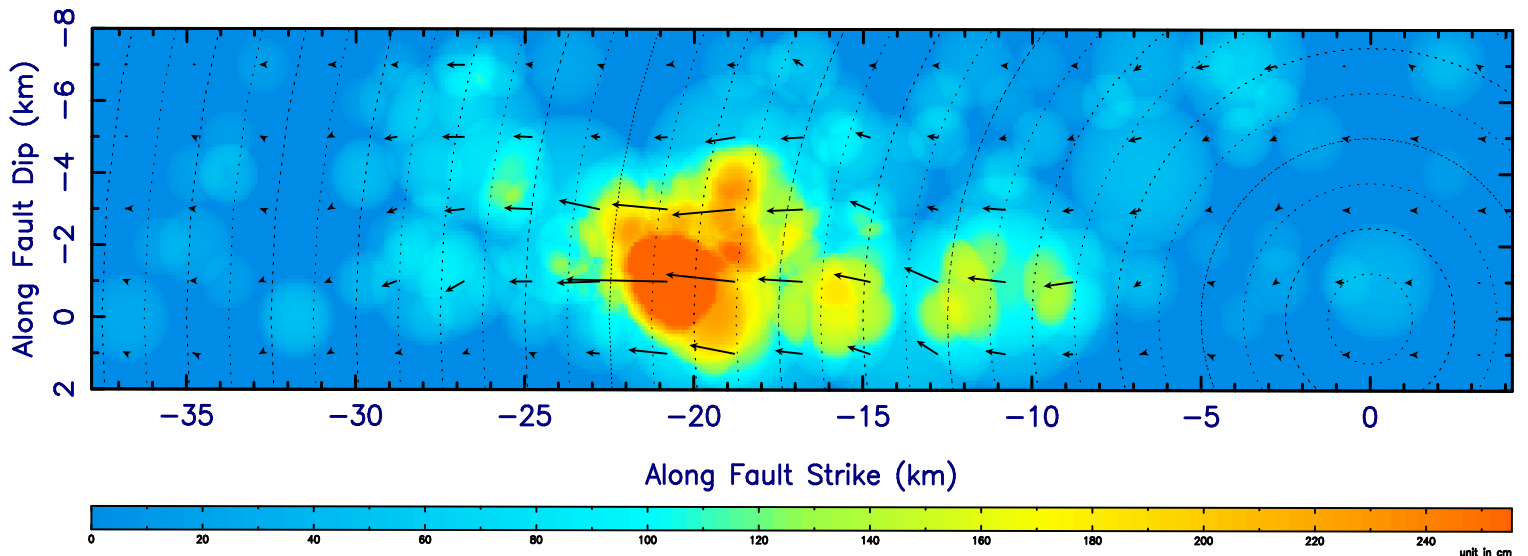


Figure 4. Schematic plot of the effective source radiation.

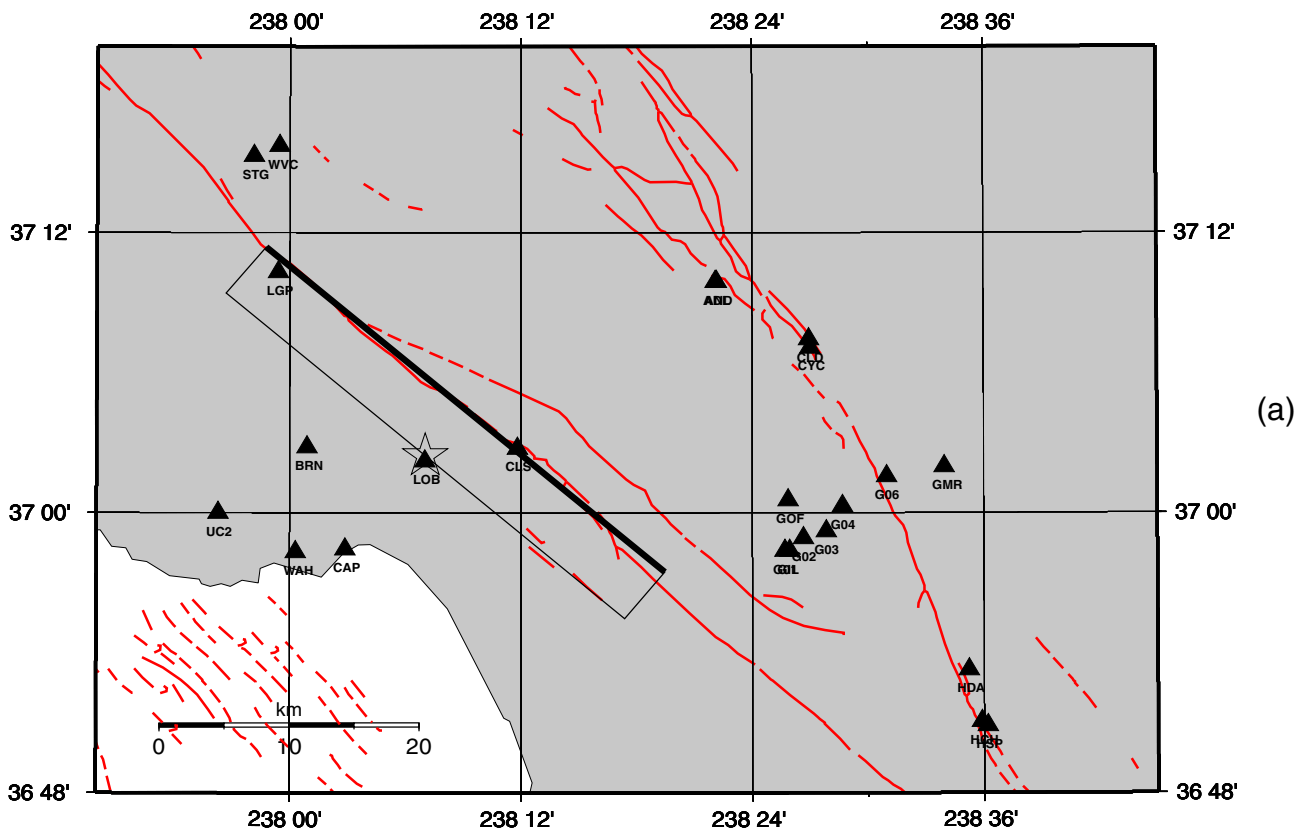


Slip Amplitude Distribution of the Imperial Valley Earthquake



(b)

Figure 5. (a) Fault geometry and stations distribution. (b) Slip distribution of the composite source model.



Slip Amplitude Distribution of the Loma Preita Earthquake

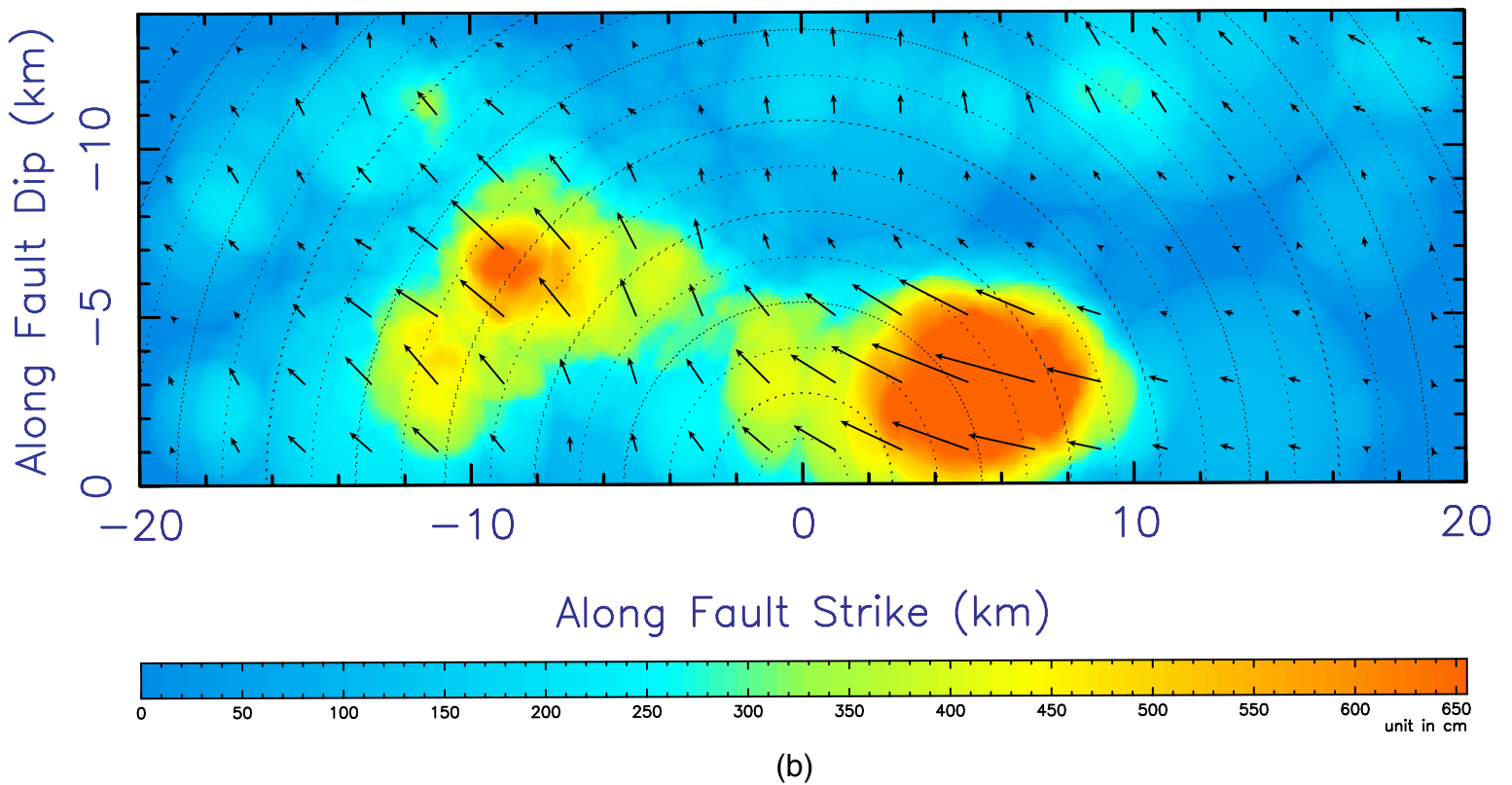
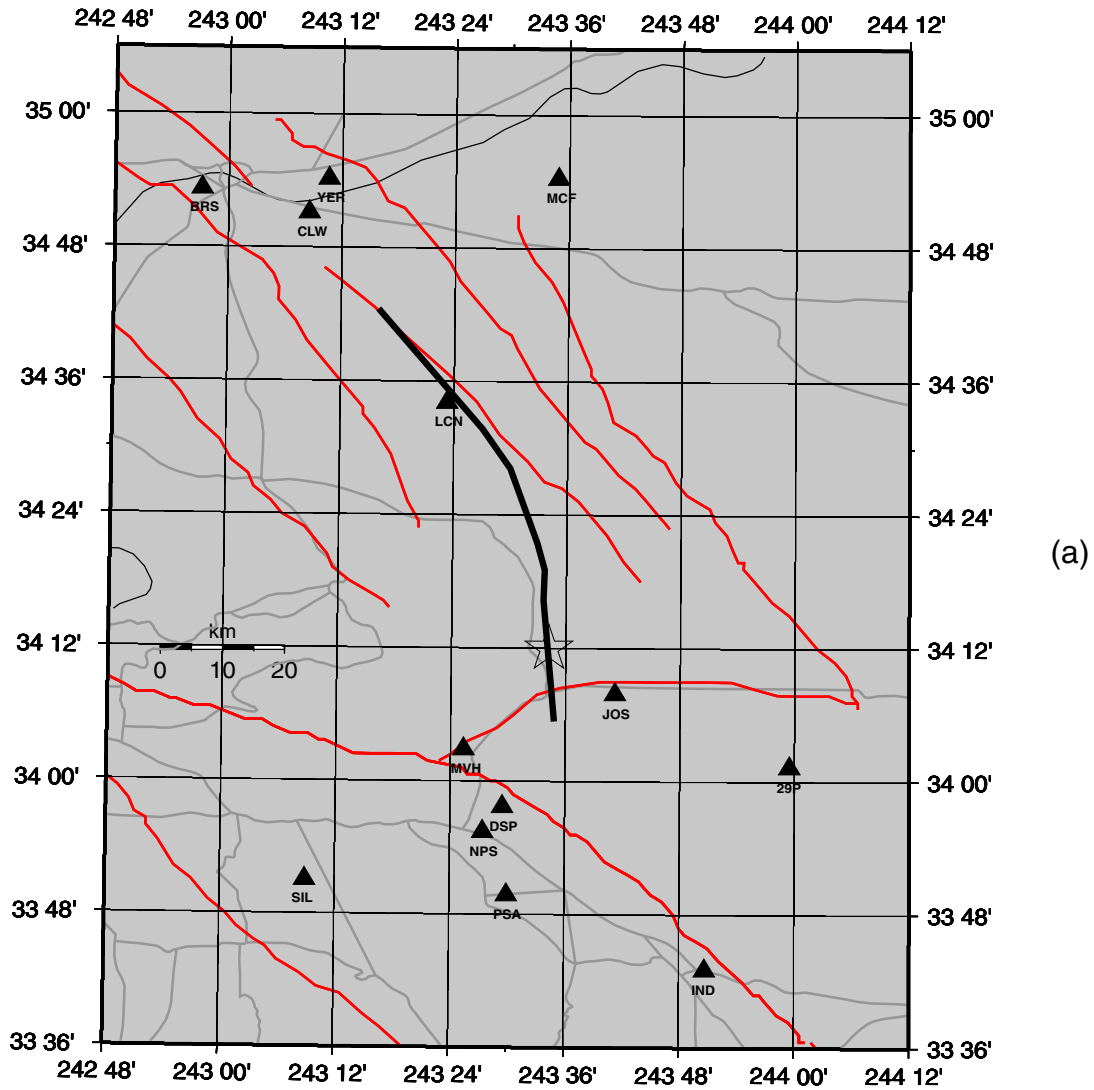


Figure 6. (a) Fault geometry and stations distribution. (b) Slip distribution of the composite source model.



Slip Amplitude Distribution of the Landers Earthquake

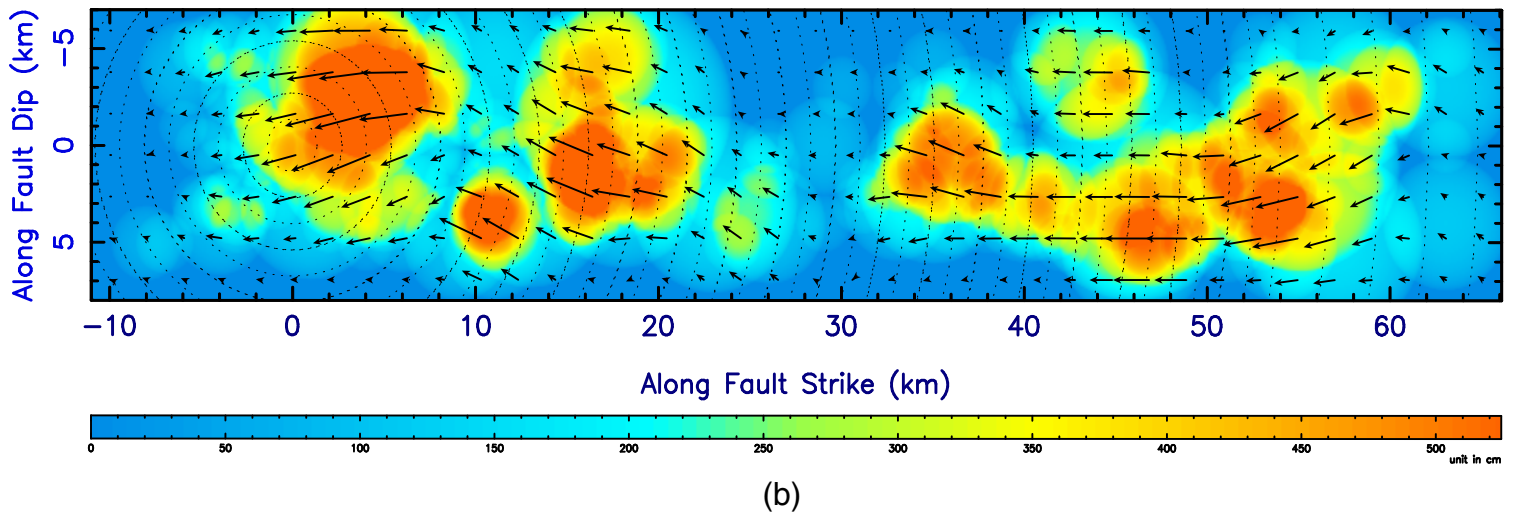
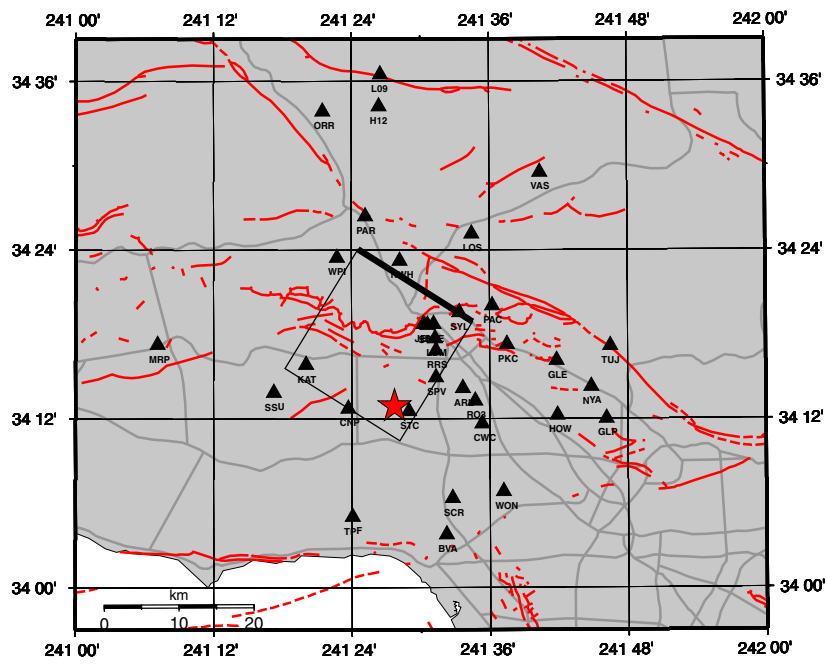
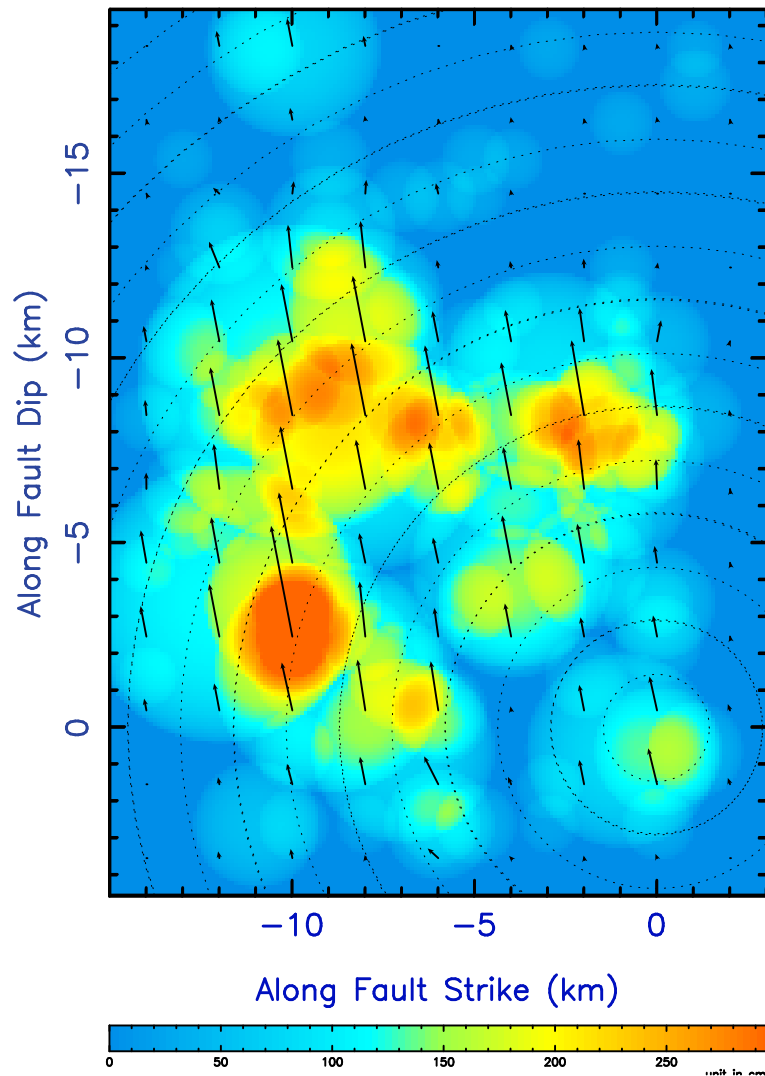


Figure 7. (a) Fault geometry and stations distribution. (b) Slip distribution of the composite source model.



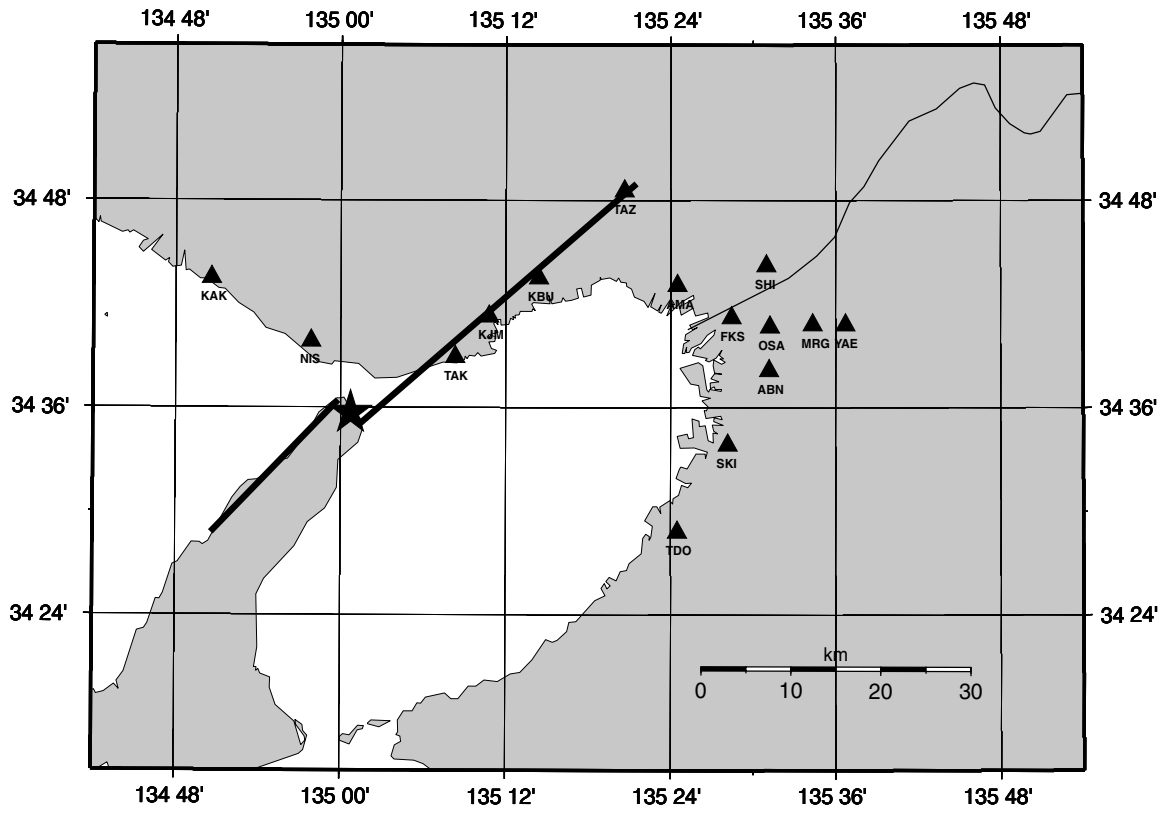
(a)

Slip amplitude distribution for the Northridge earthquake



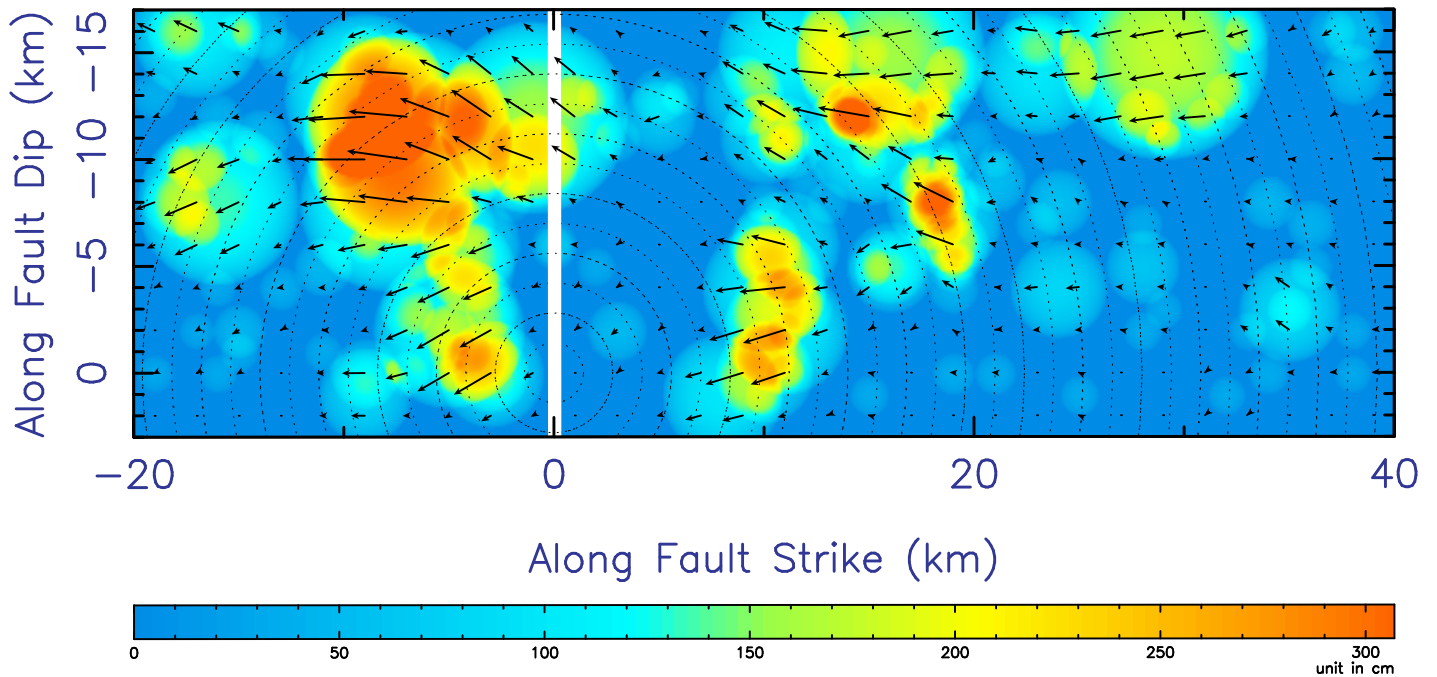
(b)

Figure 8. (a) Fault geometry and stations distribution. (b) Slip distribution of the composite source model.



(a)

Slip Amplitude Distribution for the Kobe Earthquake, Japan



(b)

Figure 9. (a) Map view of the Kobe earthquake fault geometry and strong motion station distribution. (b) Slip distribution of the composite source model for the Kobe earthquake obtained from waveform fitting between the observed and synthetic strong motion seismograms.

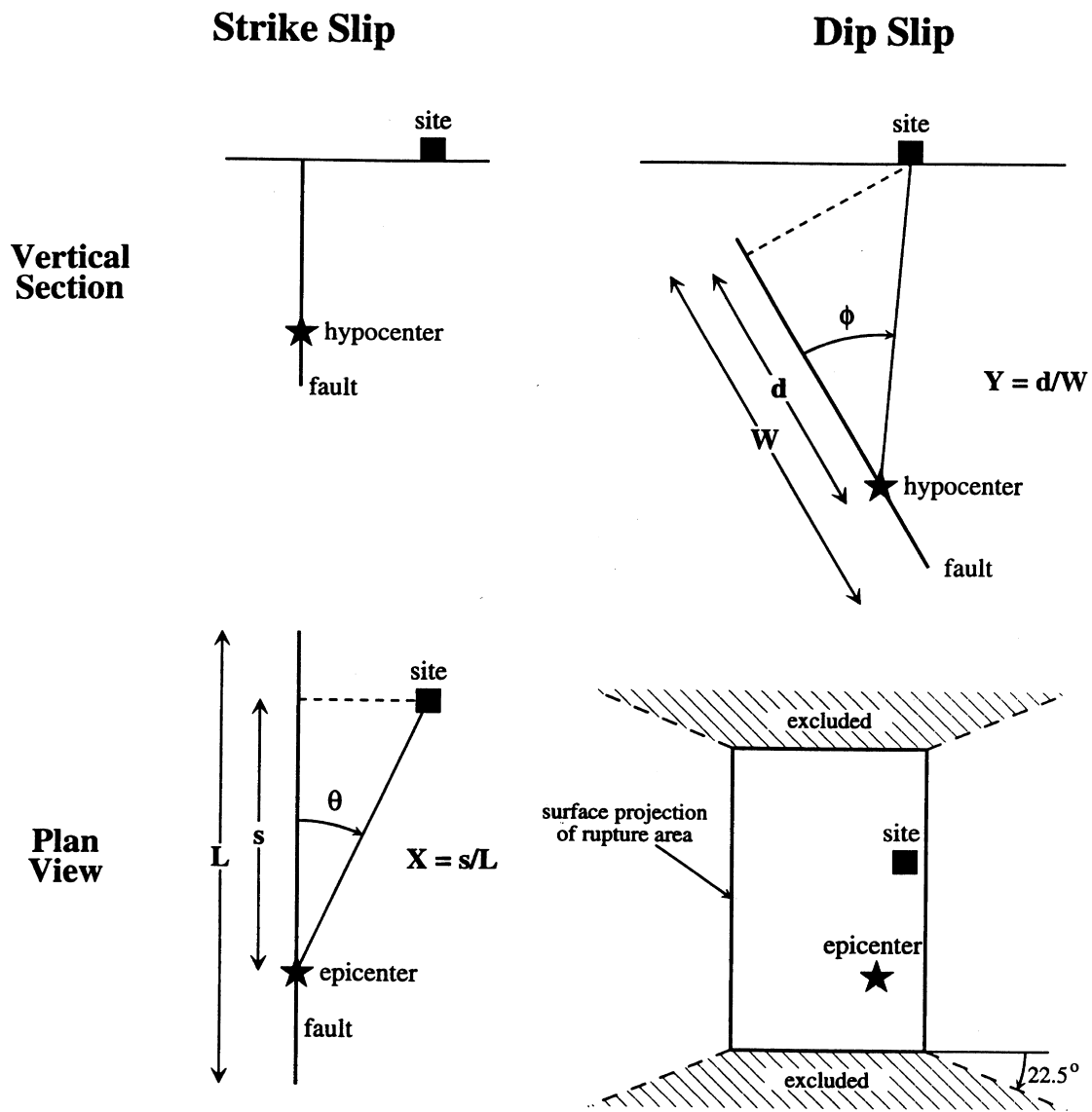


Figure 10. Geometrical configuration for fault directivity parameters from Sommerville et al. (1997).

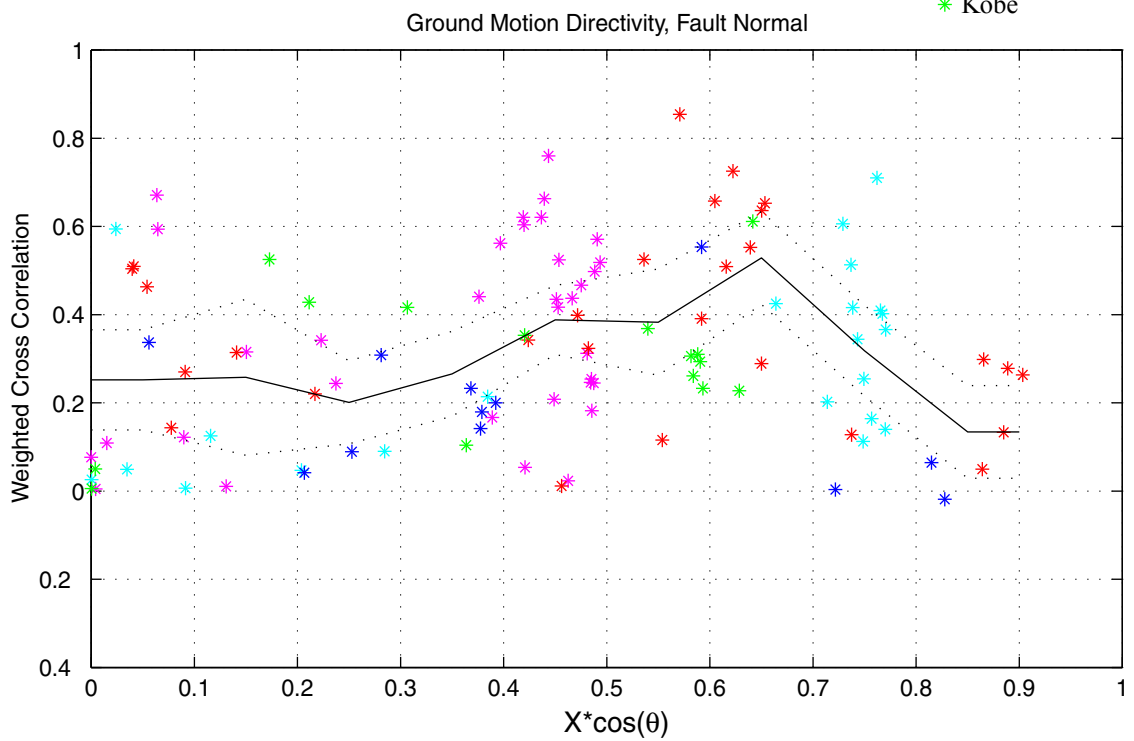
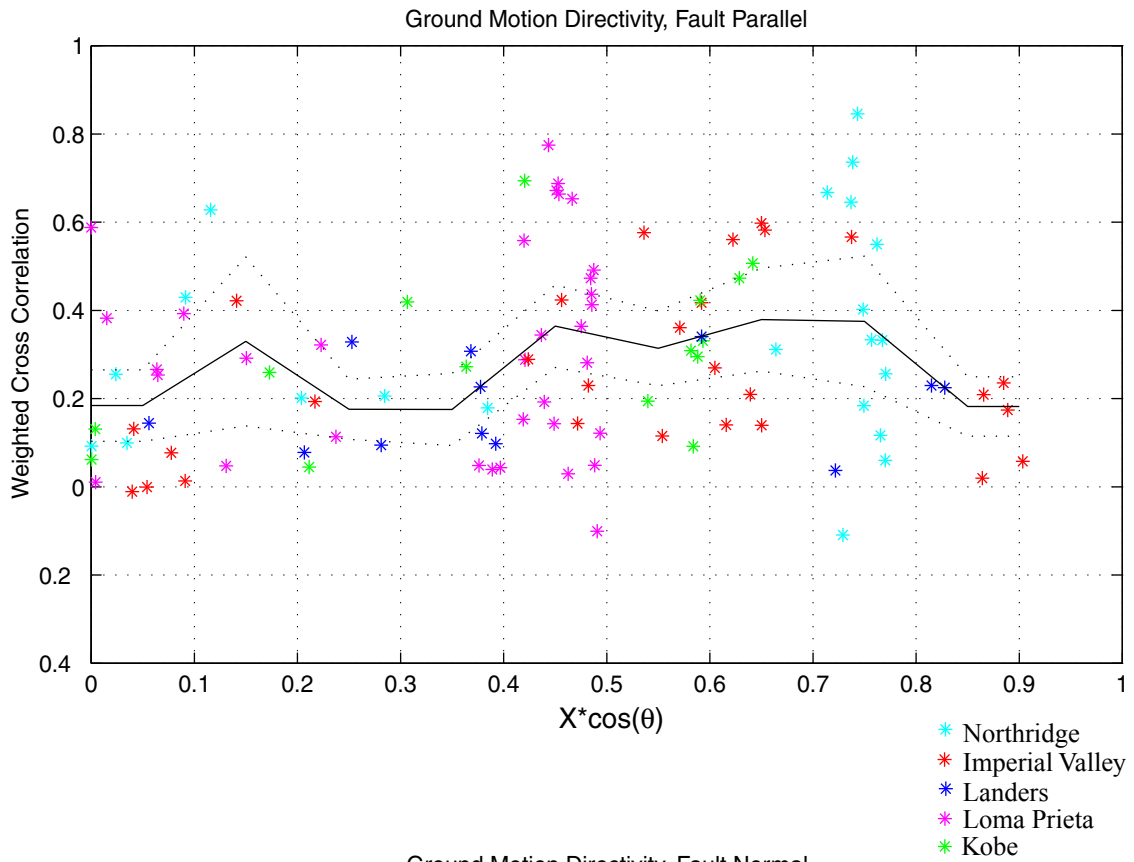


Figure 11. Effect of directivity.

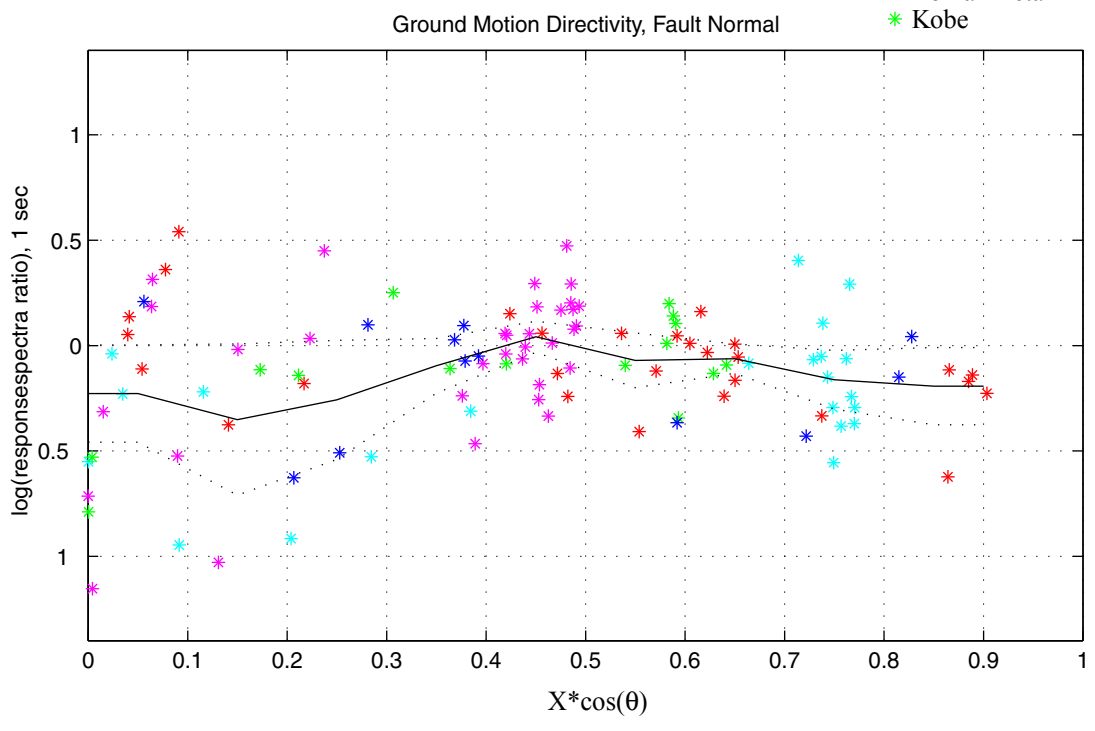
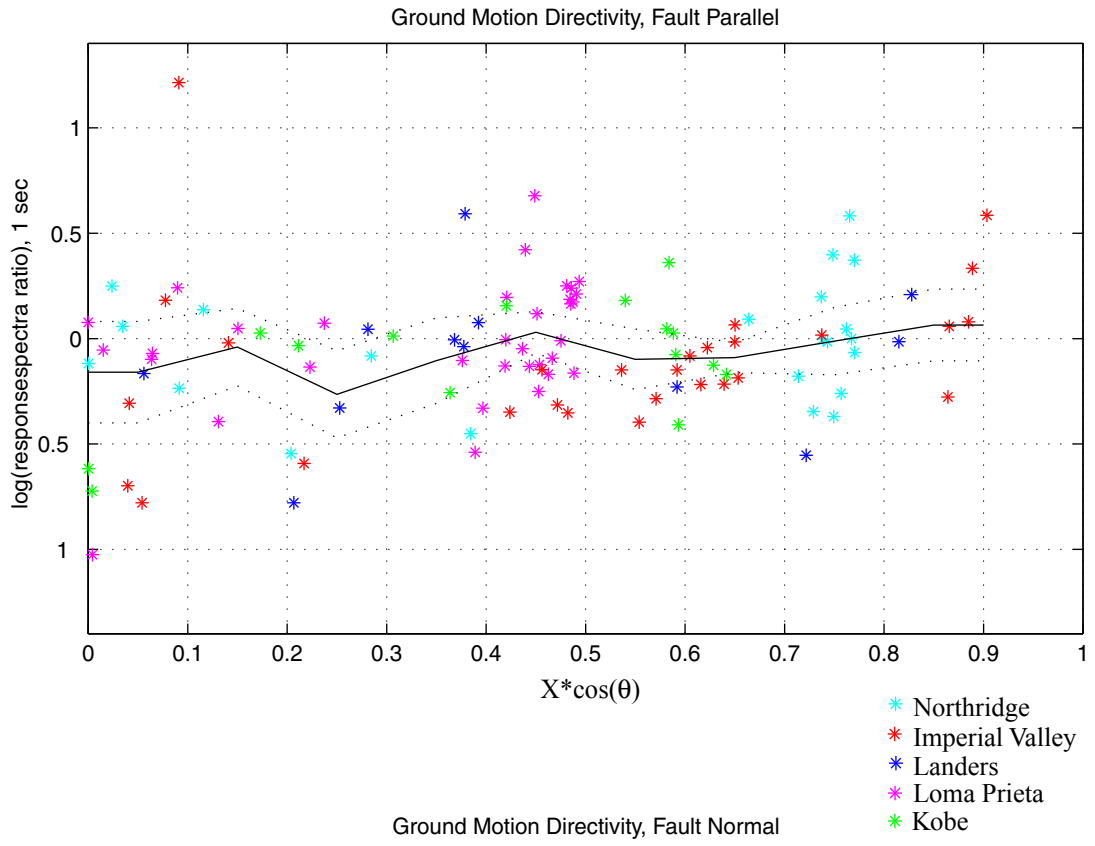


Figure 12. Effect of source directivity.

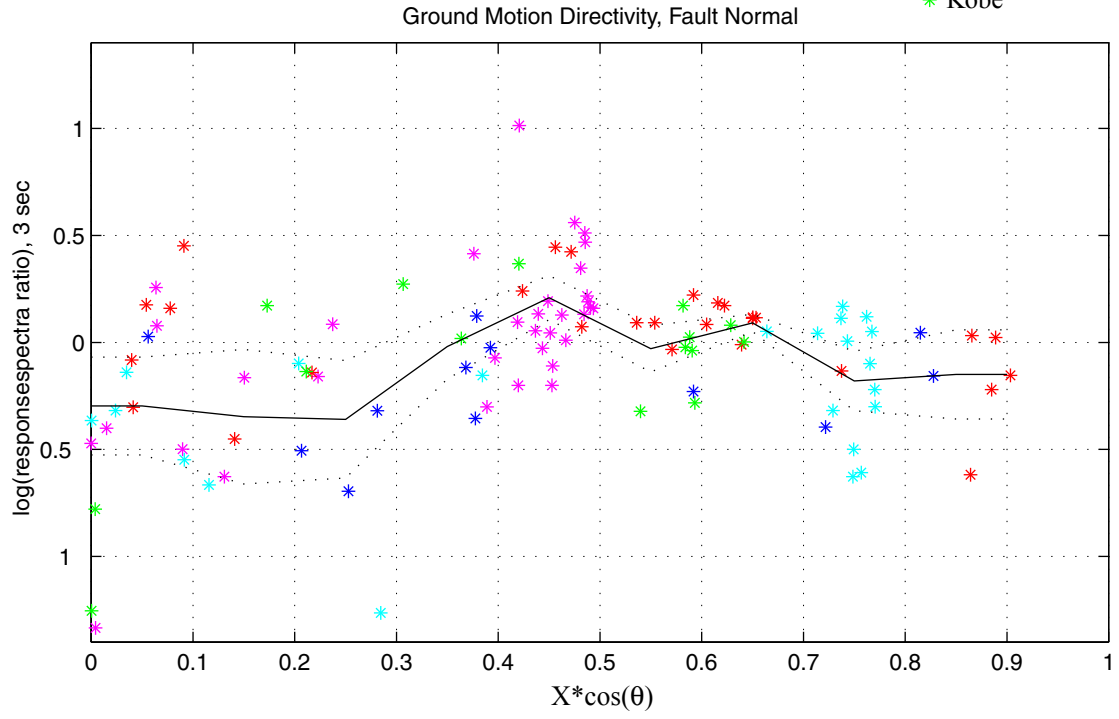
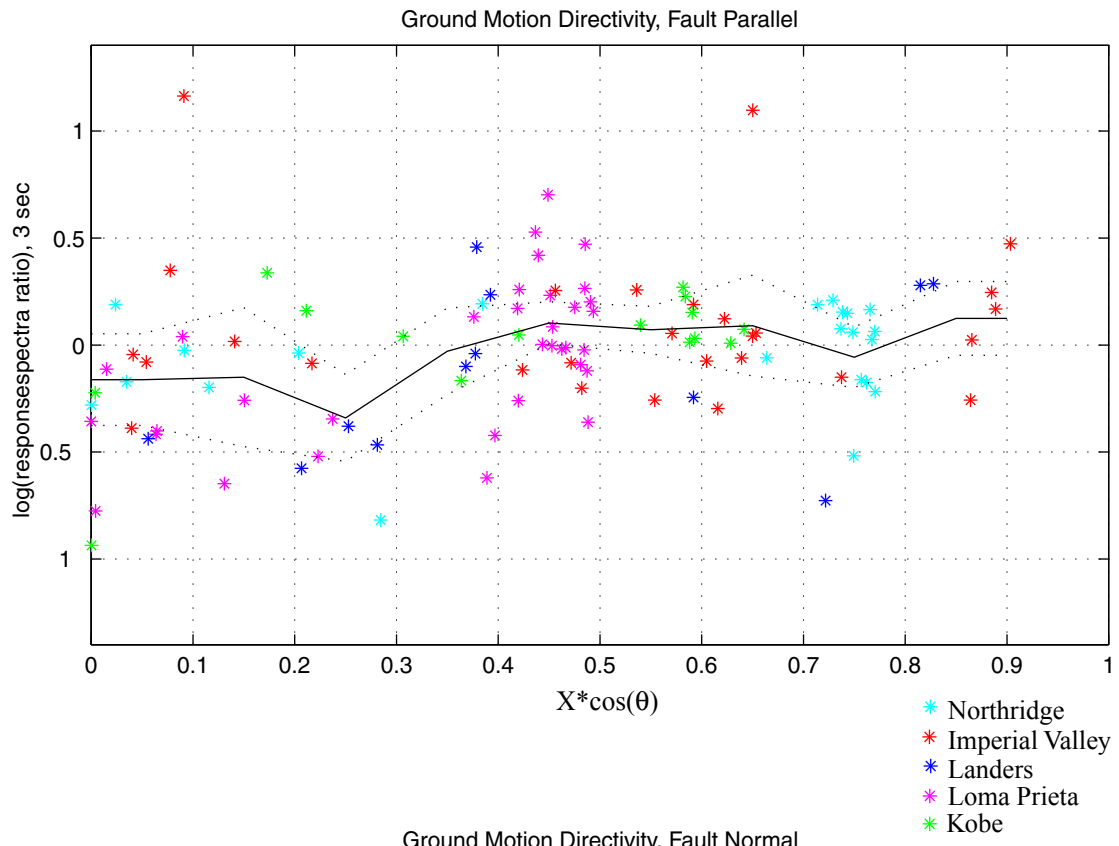


Figure 13. Effect of source directivity.

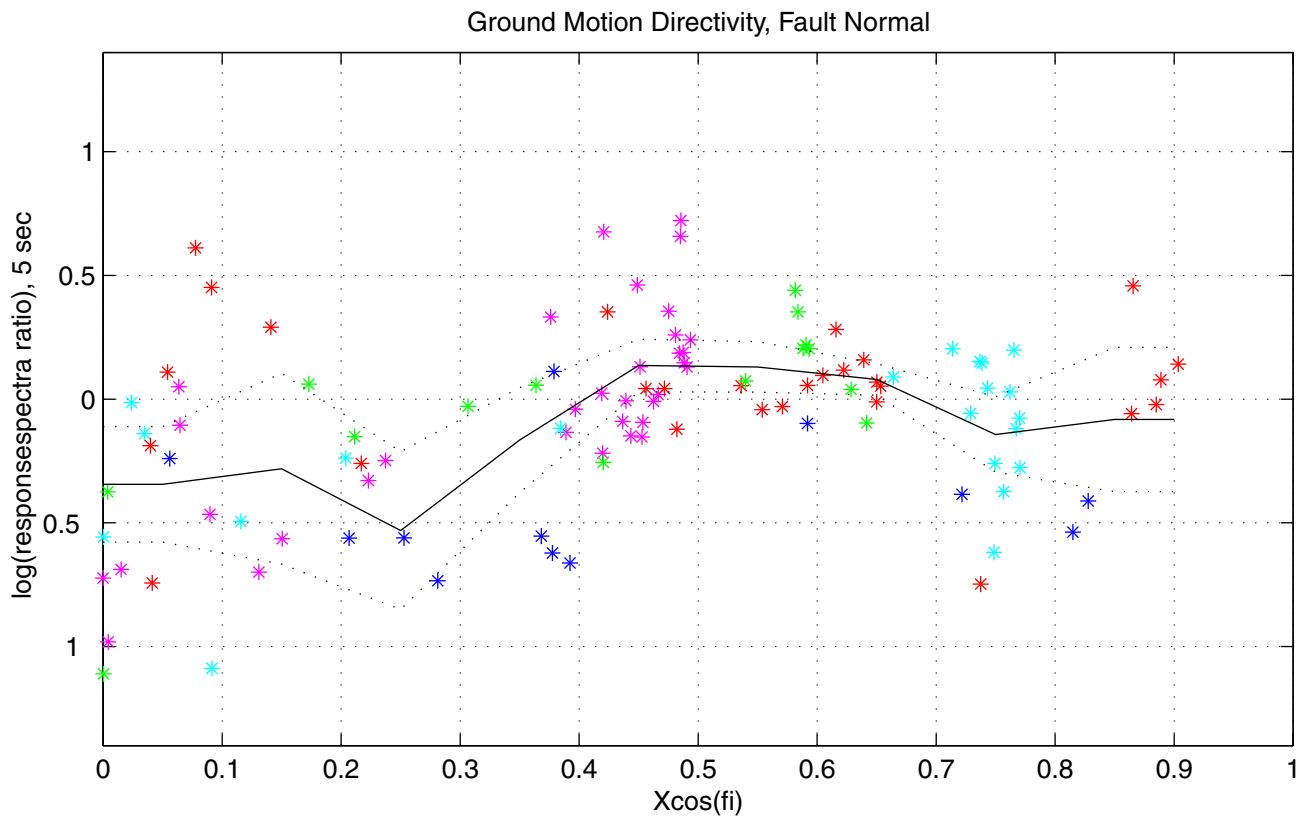
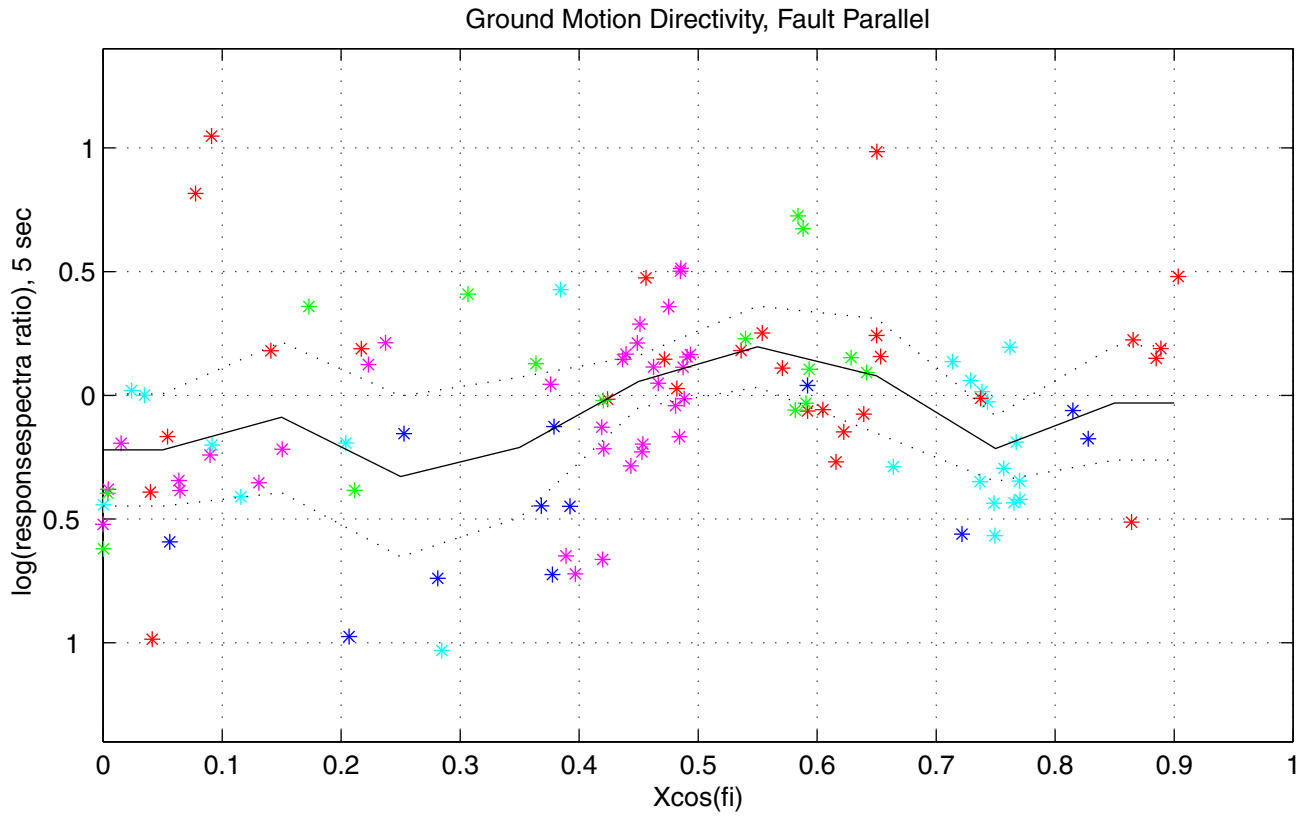


Figure 14. Effect of source directivity.